The Report Committee for Hector Domingo Escobar Alvarez
certifies that this is the approved version of the following report:

Geometrical Configuration Comparison Of Redundant Inertial Measurement Units

APPROVED BY

SUPERVISING COMMITTEE:

_____

Maruthi Akella, Supervisor

_____

Robert H. Bishop, Co-supervisor

Geometrical Configuration Comparison Of Redundant Inertial Measurement Units

by

Hector Domingo Escobar Alvarez, B.S.

REPORT

Presented to the Faculty of the Graduate School of

The University of Texas at Austin

in Partial Fulfillment

of the Requirements

for the Degree of

MASTER OF SCIENCE IN ENGINEERING

THE UNIVERSITY OF TEXAS AT AUSTIN

December 2010

Geometrical Configuration Comparison Of Redundant Inertial Measurement Units

Hector Domingo Escobar Alvarez, M.S.E.

The University of Texas at Austin, 2010

Supervisors: Maruthi Akella
               Robert H. Bishop

Inertial measurement units (IMUs) are used in a wide range of applications to estimate position, velocity, and attitude of vehicles. The high cost of tactical grade IMUs makes the low-cost microelectromechanical systems (MEMS) based IMUs appealing. These types of IMUs are less accurate, so to counteract this effect, multiple and different configurations should be used. The work presented here provides efficient and low cost solutions using different configurations of redundant (multiple) MEMS-IMU swarms, which increase the level of accuracy to potentially the order of that of a tactical IMU. Several configurations are presented and compared through different methods.

Table of Contents

List of Tables

List of Figures

Chapter 1

Introduction

1.1 Motivation

Inertial measurement units (IMUs) are used in a wide range of applications to estimate position, velocity, and attitude of vehicles in air, sea, and space. In general, these types of applications require a high level of navigational accuracy, which tactical IMUs can provide. A tactical grade IMU provides high quality measurements with low noise and high stability. However, since the cost of IMUs increases with their level of accuracy, tactical IMUs are high in cost. Currently, numerous low-cost microelectromechanical systems (MEMS) based IMUs are commercially available and have been receiving increasing attention in robotic and unmanned aircraft flight applications. These MEMS type IMUs consume less power, are smaller in size, and weigh less than tactical IMUs; however, are less accurate, drift more over time, and produce more noise in their measurements. The work presented in this report discusses efficient and low cost solutions using different configurations of redundant (multiple) MEMS-IMU swarms, increasing the level of accuracy to potentially the order of that of a tactical IMU.

Previous research has focused mainly on the optimization of multiple

single-axis accelerometers and gyros in different geometric configurations, such as cones, tetrahedrons, cubes, or pyramids [8, 12]. More recently, research using two to five IMUs on a plane has also been repeated [1]. Configurations using two IMUs, in both orthogonal and nonorthogonal configurations have been studied, as well as a skew-redundant regular tetrahedron configuration using four IMUs [3, 16]. In this report, we present several quantitavive measures to enable comparison when applied to different configurations of n number of IMUs. The different configurations include in-plane configurations, platonic solids, and half angle cone configurations.

1.2   Research Contribution

This research puts together several methods for comparing geometrical configurations of IMUs. Different configurations are presented and the figures of merit are applied to get a quantification of their optimality.

1.3   Report Organization

The theory involved in the definition of inertial navigation using strap-down technology is explained in Chapter 2. Also different geometrical solid configurations are explained in this chapter. The methods used for comparing the different configurations, together with a brief description of noise reduction is presented in Chapter 3. Specific results obtained from the application of the methods to configurations with four and eight IMUs is presented in Chapter 4. The conclusions obtained from the research are presented last in Chapter 5.

Chapter 2

Theoretical Background

2.1 Inertial Navigation

The concept of navigation comes from the desire to know the position and velocity of a vehicle. According to Newton's laws, if we are capable of measuring the acceleration of a body in an inertial reference frame, it is just a matter of integrating once to get velocity and twice to get position, given we know the initial conditions.

One way of obtaining position is known as "dead reckoning". This method takes an initial position, velocity, and IMU outputs to compute the true history to position and velocity. Knowing the initial position and velocity, the IMU measures acceleration and the rotational rates, thereby enabling the dead reckoning method. This process is known as inertial navigation since it uses inertial sensors.

Inertial navigation is usually accomplished by having measurements of three accelerometers and three gyros. The gyros are used to determine the direction in which the accelerometers are pointing in an inertial space. Before performing the integration, the output of the sensors needs to be in the correct coordinate frame.

3

2.1.1 Strapdown Inertial Navigation

In this report, strapdown inertial navigation will be used. Strapdown inertial navigation refers to the use of accelerometers and gyros rigidly mounted to the body of the vehicle [15]. This give us the versatility to mount the set of sensors in any kind of vehicle without changing any mechanical configuration.

2.1.2 Inertial Measurement Unit

The set of accelerometers and gyros form an Inertial Measurement Unit (IMU). In this report, an IMU is considered to be a set of three orthogonal accelerometers and three orthogonal gyros. The coordinate frame that they form is a right handed set. The direction of their sensing axis is shown in Figure 2.1.
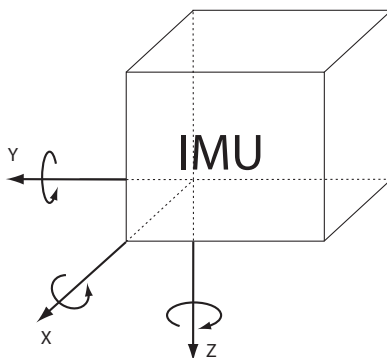
Figure 2.1: IMU Sensing Axis

2.2 Geometrical Configurations

The different basic configurations used in this work are presented. Since the IMUs are placed in different geometrical configurations, some of the platonic solids where selected, as well as cones with different half-angles, which were selected for comparison purposes.

2.2.1 Cone Configurations

The cone configurations are based on cones of half-angle denoted by α. The cone varies in its size depending on the number of IMUs used. The angle α is optimized to obtain different configurations on a cone.
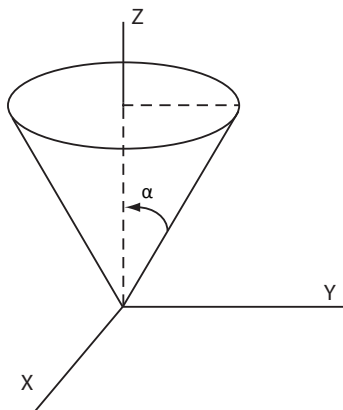
Figure 2.2: Half Angle Cone

2.2.2 Platonic Solids

The platonic solids are those formed by joining together regular polygons like the square, the triangle, and the pentagon. For example, if four

triangles are used and each set of three are joined by their vertices, a tetrahedron is formed. It has been proved [9] that only five platonic solids exist, which are the tetrahedron, the cube, the octahedron, the dodecahedron, and the icosahedron, shown in Figure 2.3.

Tetrahedron

Cube

Octahedron

Dodecahedron

Icosahedron
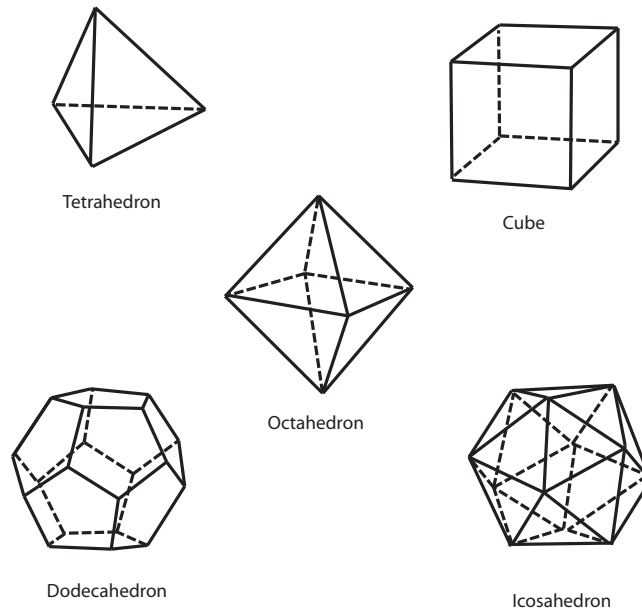
Figure 2.3: Platonic Solids

The platonic solids together with single axis sensors were studied in [12], [7], [2], among others. Geometries that have been used with IMUs are the tetrahedron (used by [14] and [16]) and half dodecahedron. In this work only the tetrahedron, the cube, and the octahedron will be considered for simplicity of the calculations, but the methodology could be applied to any configuration.

Chapter 3

Methodology for Quantifying Optimal Configuration

In this chapter, different methods to quantify the optimality of a geometrical configuration are presented. Through these methods, we are able to compare different configurations and determine which one provides more information and improved fault detection capability to the whole system.

3.1 Information Matrix

This section closely follows what was presented in [14] and in [5]. From the information filter (analogous to the Kalman filter), assuming a state space observation at time k given by

$$\mathbf{z}(k) = \mathbf{H}(k)\mathbf{x}(k) + \mathbf{v}(k),\tag{3.1}$$

the measurement covariance is defined as:

$$\mathbf{I}(k) = \mathbf{H}^T(k)\tilde{\mathbf{R}}^{-1}(k)\mathbf{H}(k)\tag{3.2}$$

where $\mathbf{x}(\mathrm{k})$ is the current state 3×1 vector of either true specific forces (which is what the accelerometers sense) or true angular rates. The $\mathbf{H}(k)$ is the observation model, and $\mathbf{v}(k)$ is the observation noise with covariance $\tilde{\mathbf{R}}(k)$. The

matrix $\mathbf{I}(k)$ is referred to as the information matrix, and provides a measure of the amount of information or the contribution of the observations to the states [5, 14].

In this context the $\mathbf{H}(k)$ matrix is made of rotation matrices (one per IMU) from a common origin to the case frame of each of the IMUs. Since the orientation of each IMU is constant and independent of time we can drop the k and write

$$\mathbf{H} = \begin{bmatrix} \mathbf{T}_{1,b}^c \\ \vdots \\ \mathbf{T}_{m,b}^c \end{bmatrix} \tag{3.3}$$

where m denotes the number of IMUs and, therefore, the number of sensors is $n = 3m$. Now, assuming that $\tilde{\mathbf{R}}(k)$ is constant and equal for all sensors, the goal is to maximize the information matrix $\mathbf{I}$

$$max\left[|\mathbf{I}|\right] = max\left[\left|\mathbf{H}^T\mathbf{H}\right|\right] \tag{3.4}$$

If $J = |\mathbf{I}|$ is maximized, the eigenvalues of J have the form

$$\lambda_i = \frac{n}{3} \tag{3.5}$$

where $i = \{1, \cdots, n\}$, and n is the number of sensors (n is the number of individual sensors and not of IMUs). Therefore:

$$J = det\left(\mathbf{H}^T\mathbf{H}\right) = \left(\frac{n}{3}\right)^3. \tag{3.6}$$

The previous result matches the one presented in [8]. J is the first comparison method, and if $J = det\left(\mathbf{H}^T\mathbf{H}\right)$ in Eq. (3.6) is evaluated, then

the result is based purely on the geometry of the sensors. If $J = \left(\frac{n}{3}\right)^3$. is evaluated, then J depends only on the number of sensors used. In [6] and [5] it was shown that J, defined in Eq. (3.6), depends only on the number of sensors and therefore is not a very useful result when evaluating different IMU configurations with the same number of sensors.

3.2 Partial Redundancy

This method was introduced as a reliability criterion for geodetic networks by [13]. Later it was used in [5] for comparing IMUs configurations. The criterion is based on the diagonal elements of the matrix $\mathbf{Z}$ defined as:

$$\mathbf{Z} = \mathbf{I}_n - \mathbf{H}\left(\mathbf{H}^T\tilde{\mathbf{R}}^{-1}\mathbf{H}\right)^{-1}\mathbf{H}^T\tilde{\mathbf{R}}^{-1} \tag{3.7}$$

The goal is to minimize the standard deviation of the elements $\mathbf{z}$, formed by the diagonal elements of the $\mathbf{Z}$ matrix. That is

$$\tilde{J} = min\sqrt{E[(\mathbf{z} - E[\mathbf{z}])^2]} \tag{3.8}$$

Also, [6] showed that the summation of the diagonal elements z_i remains constant and equal to

$$\sum_{i=1}^{n} z_i = 3(\frac{n}{3} - 1) = n - 3 \tag{3.9}$$

which again shows that these parameters are dependent on the number of sensors only.

3.3   Augmented Observation Model Matrix $\tilde{\mathbf{H}}$

The previous methods considered only the number of sensors and not the geometry, therefore another figure of merit is needed. For this, a different definition of the $\mathbf{H}(k)$ matrix is required.

It is known that accelerometers measure specific force and not accelerations. The specific force is defined as the sum of the kinematic acceleration $\mathbf{a}$ and the gravitational acceleration $\mathbf{g}$, or

$$\mathbf{f} = \mathbf{a} - \mathbf{g} \tag{3.10}$$

Consider the acceleration $\mathbf{a}_i$ at a point on a rigid body at position $\mathbf{r}_i$. If the origin of the body frame has an accelerations $\mathbf{a}$ and an angular rate $\boldsymbol{\omega}$, the acceleration on that point could be expressed as [7]:

$$\mathbf{a}_i = \mathbf{a} + \dot{\boldsymbol{\omega}} \times \mathbf{r}_i + \boldsymbol{\omega} \times (\boldsymbol{\omega} \times \mathbf{r}_i) \tag{3.11}$$

The specific force is

$$\mathbf{f}_i = \mathbf{a} + \dot{\boldsymbol{\omega}} \times \mathbf{r}_i + \boldsymbol{\omega} \times (\boldsymbol{\omega} \times \mathbf{r}_i) - \mathbf{g} \tag{3.12}$$

Define the orientation vector of a given single axis accelerometer, from the origin of the body frame as $\mathbf{d}_i$. From [7], the measurement y_i of a single axis accelerometer is

$$y_i = \mathbf{d}_i \cdot \mathbf{a} + (\dot{\boldsymbol{\omega}} \times \mathbf{r}_i) \cdot \mathbf{d}_i + [\boldsymbol{\omega} \times (\boldsymbol{\omega} \times \mathbf{r}_i)] \cdot \mathbf{d}_i - \mathbf{d}_i \cdot \mathbf{g} \tag{3.13}$$

Defining the skew symmetric forms of $\boldsymbol{\omega}$ and $\mathbf{r}_i$ respectively as

$$\boldsymbol{\Omega} = \begin{bmatrix} 0 & -\omega_3 & \omega_2 \\ \omega_3 & 0 & -\omega_1 \\ \omega_2 & \omega_1 & 0 \end{bmatrix} \quad \boldsymbol{\Gamma_i} = \begin{bmatrix} 0 & -r_{i_z} & r_{i_y} \\ r_{i_z} & 0 & -r_{i_x} \\ r_{i_y} & r_{i_x} & 0 \end{bmatrix} ,$$

the second and third terms of Eq. (3.13) can be written as

$$\mathbf{d}_i \cdot (\dot{\boldsymbol{\omega}} \times \mathbf{r}_i) = -\mathbf{d}_i^T \boldsymbol{\Gamma}_i \dot{\boldsymbol{\omega}} \tag{3.14}$$

$$[\boldsymbol{\omega} \times (\boldsymbol{\omega} \times \mathbf{r}_i)] \cdot \mathbf{d}_i = \mathbf{d}_i^T \boldsymbol{\Omega}^2 \mathbf{r}_i \tag{3.15}$$

and Eq. (3.13) reduces to

$$y_i = \mathbf{a} \cdot \mathbf{d}_i - \mathbf{d}_i^T \boldsymbol{\Gamma}_i \dot{\boldsymbol{\omega}} + \mathbf{d}_i^T \boldsymbol{\Omega}^2 \mathbf{r}_i - \mathbf{d}_i \cdot \mathbf{g} \tag{3.16}$$

Finally, stacking several measurements of Eq. (3.16) result in

$$\mathbf{y} = \tilde{\mathbf{H}}\mathbf{x} + \begin{pmatrix} \mathbf{d}_1^T \boldsymbol{\Omega}^2 \mathbf{r}_1 \\ \vdots \\ \mathbf{d}_n^T \boldsymbol{\Omega}^2 \mathbf{r}_n \end{pmatrix} + \begin{bmatrix} \mathbf{d}_1^T \\ \vdots \\ \mathbf{d}_1^T \end{bmatrix} \cdot \mathbf{g} \tag{3.17}$$

where

$$\mathbf{x} = \begin{pmatrix} \dot{\boldsymbol{\omega}} \\ \mathbf{a} \end{pmatrix} \tag{3.18}$$

and

$$\tilde{\mathbf{H}} = \begin{bmatrix} (\mathbf{r}_1 \times \mathbf{d}_1)^T & \vdots & \mathbf{d}_1^T \\ \vdots & \vdots & \vdots \\ (\mathbf{r}_n \times \mathbf{d}_n)^T & \vdots & \mathbf{d}_n^T \end{bmatrix} \tag{3.19}$$

In this case, n is also the number of single sensors. The matrix $\tilde{\mathbf{H}}$ considers the amount of information that the accelerometers contribute to the angular acceleration. The angular acceleration can be integrated to get angular rates that can then be compared to the actual measurements.

For simplicity, the position and orientation vectors $\mathbf{r_i}$ and $\mathbf{d_i}$ will be stacked into two matrices $\mathbf{R}$ and $\mathbf{D}$, respectively. Three vectors of position

and three vectors of orientation are needed for each IMU since each IMU has three pairs of gyros and accelerometers.

3.4   Conditioning Number

Consider a simple linear system of algebraic equations that has a unique solution $\mathbf{x}$:

$$\mathbf{H}\mathbf{x} = \mathbf{b} \tag{3.20}$$

If we add a "small" perturbation $\delta\mathbf{b}$ to $\mathbf{b}$, it will also have a solution near to $\mathbf{x}$. Denoting this solution as $\mathbf{x} + \delta\mathbf{x}$, we can write

$$\mathbf{H}\left(\mathbf{x} + \delta\mathbf{x}\right) = \left(\mathbf{b} + \delta\mathbf{b}\right) \tag{3.21}$$

which can be reduced using Eq. (3.20) to

$$\mathbf{H}\delta\mathbf{x} = \delta\mathbf{b} \tag{3.22}$$

Since $\mathbf{H}$ may not be square, the singular value decomposition $\mathbf{H} = \mathbf{U}\boldsymbol{\Sigma}\mathbf{V}^{T}$ will be used. The matrices $\mathbf{U}$ and $\mathbf{V}$ are orthonormal matrices and the diagonal matrix $\boldsymbol{\Sigma}$ is formed by the square roots of the eigenvalues of $\mathbf{H}^{T}\mathbf{H}$, which are the singular values of $\mathbf{H}$. Also, we need to define the largest and smallest singular value of $\mathbf{H}$ as $\bar{\sigma}(\mathbf{H})$ and $\underline{\sigma}(\mathbf{H})$, respectively. With this decomposition, Eq. (3.20) and Eq. (3.22) can be written as

$$\mathbf{U}\boldsymbol{\Sigma}\mathbf{V}^{T}\mathbf{x} = \mathbf{b} \tag{3.23}$$

and

$$\mathbf{U}\boldsymbol{\Sigma}\mathbf{V}^{T}\delta\mathbf{x} = \delta\mathbf{b} \tag{3.24}$$

Rearranging Eq. (3.24)

$$\delta\mathbf{x} = \mathbf{V}\mathbf{\Sigma}^{-1}\mathbf{U}^T\delta\mathbf{b} \tag{3.25}$$

Applying the induced matrix norm to Eq. (3.23) and to Eq. (3.25) yields the following two equations

$$
\begin{aligned}
\|\mathbf{b}\| &\leq \|\mathbf{U}\mathbf{\Sigma}\mathbf{V}^T\|\|\mathbf{x}\| \\
&\leq \bar{\sigma}(\mathbf{H})\|\mathbf{x}\|
\end{aligned} \tag{3.26}
$$

$$
\begin{aligned}
\|\delta\mathbf{x}\| &\leq \|\mathbf{V}\mathbf{\Sigma}^{-1}\mathbf{U}^T\|\|\delta\mathbf{b}\| \\
&\leq \frac{1}{\underline{\sigma}(\mathbf{H})}\|\delta\mathbf{b}\|
\end{aligned} \tag{3.27}
$$

Rearranging Eq. (3.26) yields

$$\frac{1}{\|\mathbf{x}\|} \leq \bar{\sigma}(\mathbf{H})\frac{1}{\|\mathbf{b}\|} \tag{3.28}$$

and multiplying by Eq. (3.27) gives the following relationship:

$$\frac{\|\delta\mathbf{x}\|}{\|\mathbf{x}\|} \leq \frac{\bar{\sigma}(\mathbf{H})}{\underline{\sigma}(\mathbf{H})}\frac{\|\delta\mathbf{b}\|}{\|\mathbf{b}\|} \tag{3.29}$$

The ratios $\frac{\|\delta\mathbf{x}\|}{\|\mathbf{x}\|}$ and $\frac{\|\delta\mathbf{b}\|}{\|\mathbf{b}\|}$ represent the relative sizes of the perturbations with respect to $\mathbf{b}$ and $\mathbf{x}$, respectively. Therefore it is desired that if $\frac{\|\delta\mathbf{x}\|}{\|\mathbf{x}\|}$ is small, then $\frac{\|\delta\mathbf{b}\|}{\|\mathbf{b}\|}$ be small as well. Eq. (3.29) thus provides bounds for $\frac{\|\delta\mathbf{x}\|}{\|\mathbf{x}\|}$ in terms of $\frac{\|\delta\mathbf{b}\|}{\|\mathbf{b}\|}$.

If $\frac{\bar{\sigma}(\mathbf{H})}{\underline{\sigma}(\mathbf{H})}$ is small, then small values of $\frac{\|\delta\mathbf{b}\|}{\|\mathbf{b}\|}$ will in turn yield small values of $\frac{\|\delta\mathbf{x}\|}{\|\mathbf{x}\|}$, which is what is needed. In contrast, if $\frac{\bar{\sigma}(\mathbf{H})}{\underline{\sigma}(\mathbf{H})}$ is large we might obtain large values of $\frac{\|\delta\mathbf{x}\|}{\|\mathbf{x}\|}$. The value of

$$k = \frac{\bar{\sigma}(\mathbf{H})}{\underline{\sigma}(\mathbf{H})} \tag{3.30}$$

is called the condition number. The use of this method was first presented in [11], but applied only applied to GPS. Later on, this theory was applied to IMUs [7]. Applying this definition to the $\tilde{\mathbf{H}}$ matrix defined in Eq. (3.19), the condition number k can be also defined as:

$$k(\tilde{\mathbf{H}}) = \sqrt{\frac{\lambda_{max}\left(\tilde{\mathbf{H}}^T\tilde{\mathbf{H}}\right)}{\lambda_{min}\left(\tilde{\mathbf{H}}^T\tilde{\mathbf{H}}\right)}} = \|\tilde{\mathbf{H}}^T\tilde{\mathbf{H}}\|\| (\tilde{\mathbf{H}}^T\tilde{\mathbf{H}})^{-1}\| \qquad (3.31)$$

wherein $\lambda_{max}(\mathbf{M})$ and $\lambda_{min}(\mathbf{M})$ are respectively the largest and smallest eigenvalues for any symmetric matrix $\mathbf{M}$. This condition number indicates how close $\tilde{\mathbf{H}}^T\tilde{\mathbf{H}}$ is to singularity and shows the maximum possible impact of the measurement errors on the system accuracy, therefore this value should, preferably always be kept small.

3.5 Dilution of Precision

The Geometric Dilution of Precision (GDOP) concept relates the effect of GPS satellite geometry with GPS precision. The same concept was applied to the $\tilde{\mathbf{H}}$ matrix in Eq. (3.19) as follows [7]:

$$GDOP\left(\tilde{\mathbf{H}}\right) \equiv \sqrt{tr\left(\tilde{\mathbf{H}}^T\tilde{\mathbf{H}}\right)^{-1}} \qquad (3.32)$$

Furthermore, if we partition $\tilde{\mathbf{H}}$ in its angular and linear acceleration parts as in Eq. (3.19)

$$\tilde{\mathbf{H}} = \left[\begin{array}{ccc} \mathbf{H}_{\dot{\omega}_{3\times n}} & \vdots & \mathbf{H}_{a_{3\times n}} \end{array} \right] \qquad (3.33)$$

we can define *Angular Dilution of Precision* as

$$\dot\omega DOP\left(\tilde{\mathbf{H}}\right) \equiv \sqrt{tr\left(\mathbf{H_{\dot\omega}}^T\mathbf{H_{\dot\omega}}\right)^{-1}} \tag{3.34}$$

and *Acceleration Dilution of Precision*

$$aDOP\left(\tilde{\mathbf{H}}\right) \equiv \sqrt{tr\left(\mathbf{H_a}^T\mathbf{H_a}\right)^{-1}} \tag{3.35}$$

It is important to note that $\mathbf{H_a} = \mathbf{H}$, as defined in Eq. (3.3). The DOP values also give a sense of how close to singularity $\tilde{\mathbf{H}}^T\tilde{\mathbf{H}}$ is. The reasoning is because the trace of $(\tilde{\mathbf{H}}^T\tilde{\mathbf{H}})^{-1}$ can be written as

$$Tr(\tilde{\mathbf{H}}^T\tilde{\mathbf{H}})^{-1} = \sum_{i=1}^{N}\frac{1}{\lambda_i\left(\tilde{H}^T\tilde{H}\right)} \tag{3.36}$$

We notice that if any eigenvalue is close to zero, the DOP value will be high, which is why the dilution of precision values should be kept small.

Chapter 4

Results of Configuration Performance

In this chapter we present the results of applying the different figures of merit described in Chapter 3 to several geometrical configurations. Configurations using four, eight, and twelve sets of IMUs are presented.

4.1 Configurations with Four IMUs

This section presents the use of four IMUs to generate different configurations. Later a comparison table shows their performance according to the different figures of merit.

4.1.1 Four IMUs on a Plane

This configuration has four IMUs placed on a plane. They form a square where each of the position vectors is a unit vector, as seen in Figure 4.1
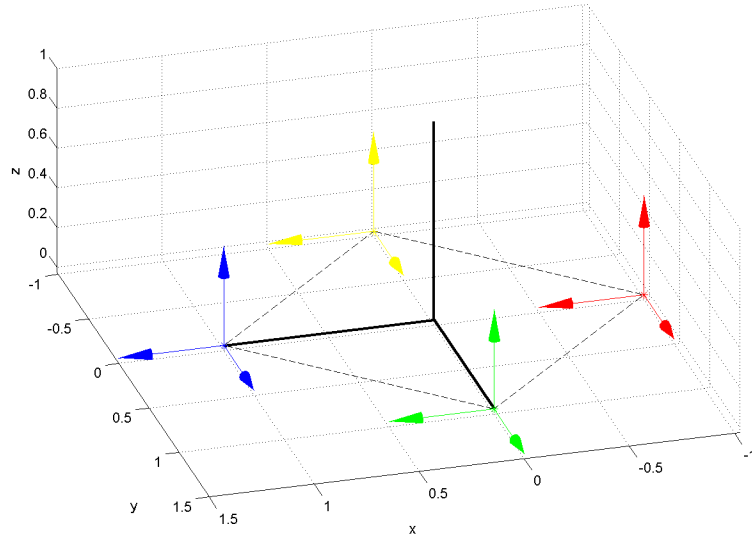
Figure 4.1: Four IMUs on a plane

The rows of $\mathbf{R}$ represent the position from the origin of the body frame to the origin of the case frame of each sensor, while the $\mathbf{D}$ matrix represents its orientation. These two matrices are used to construct $\mathbf{H}$ and $\tilde{\mathbf{H}}$. Since three sensors form an IMU, three consecutive rows of $\mathbf{R}$ will be identical. This is because the sensors of each IMU have the same origin. However, they have different orientation, and therefore the corresponding three rows of $\mathbf{D}$ will be

17

different. The sensors are placed on the corners of a square.

$$\mathbf{R} = \begin{bmatrix} 1 & 0 & 0 \\ 1 & 0 & 0 \\ 1 & 0 & 0 \\ 0 & 1 & 0 \\ 0 & 1 & 0 \\ 0 & 1 & 0 \\ 0 & -1 & 0 \\ 0 & -1 & 0 \\ 0 & -1 & 0 \\ -1 & 0 & 0 \\ -1 & 0 & 0 \\ -1 & 0 & 0 \end{bmatrix} \quad \mathbf{D} = \begin{bmatrix} 1 & 0 & 0 \\ 0 & 1 & 0 \\ 0 & 0 & 1 \\ 1 & 0 & 0 \\ 0 & 1 & 0 \\ 0 & 0 & 1 \\ 1 & 0 & 0 \\ 0 & 1 & 0 \\ 0 & 0 & 1 \\ 1 & 0 & 0 \\ 0 & 1 & 0 \\ 0 & 0 & 1 \end{bmatrix} \tag{4.1}$$

When the figures of merit are computed for this configuration, we obtain the values in Table 4.1.

Table 4.1: Figures of Merit for a Square

	J	$\tilde{J}$	k	GDOP	$\dot{\omega}$DOP	aDOP
Plane	64	0	1.4142	1.4142	1.1180	0.8660

If the orientation of the sensing axis is pointed such that two of the axis form the square and the remaining points up, as illustrated in Figure 4.2, the results of the figures of merit do not change and remain the same as in Table 4.1.
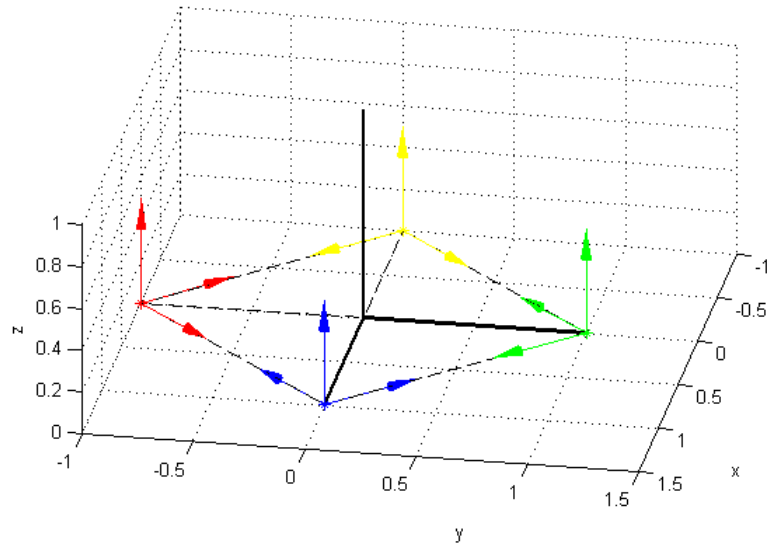
18

Figure 4.2: Square formed with 4 IMUs in a plane

4.1.2 Four IMUs Equally Distributed on a Cone

Figure 4.3 shows a cone with a half angle $\alpha = 54.72^o$. The IMUs are equally distributed along the surface of the cone.
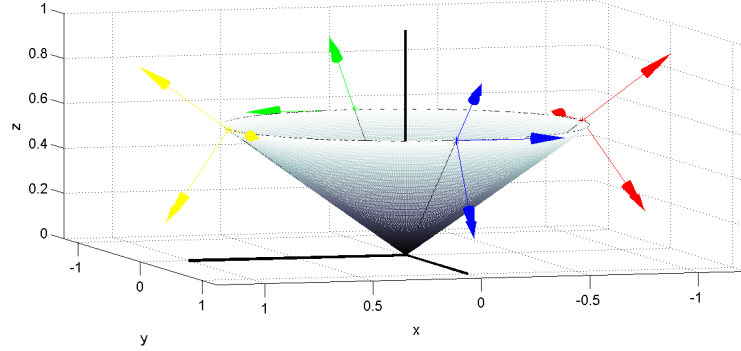
Figure 4.3: Four IMUs Equally Distributed on Cone

Their positions and directions are represented by the two matrices in Eq. (4.2), in terms of the half angle α.

$$\mathbf{R} = \begin{bmatrix} 0 & \sin\alpha & \cos\alpha \\ 0 & \sin\alpha & \cos\alpha \\ 0 & \sin\alpha & \cos\alpha \\ -\sin\alpha & 0 & \cos\alpha \\ -\sin\alpha & 0 & \cos\alpha \\ -\sin\alpha & 0 & \cos\alpha \\ 0 & -\sin\alpha & \cos\alpha \\ 0 & -\sin\alpha & \cos\alpha \\ 0 & -\sin\alpha & \cos\alpha \\ \sin\alpha & 0 & \cos\alpha \\ \sin\alpha & 0 & \cos\alpha \\ \sin\alpha & 0 & \cos\alpha \end{bmatrix} \quad \mathbf{D} = \begin{bmatrix} 0 & \cos\alpha & -\sin\alpha \\ -1 & 0 & 0 \\ 0 & \sin\alpha & \cos\alpha \\ -\cos\alpha & 0 & -\sin\alpha \\ 0 & -1 & 0 \\ -\sin\alpha & 0 & \cos\alpha \\ 0 & -\cos\alpha & -\sin\alpha \\ 1 & 0 & 0 \\ 0 & -\sin\alpha & \cos\alpha \\ \cos\alpha & 0 & -\sin\alpha \\ 0 & 1 & 0 \\ \sin\alpha & 0 & \cos\alpha \end{bmatrix}$$

(4.2)

Using $\alpha = 54^o$, yields the results in Table 4.2.

Table 4.2: Figures of Merit for Cone with Four IMUs with $\alpha = 54^o$

	J	$\tilde{J}$	k	GDOP	$\dot{\omega}$DOP	aDOP
4 Equally spaced	64	0	2.4853	1.7682	1.0607	0.8660

In order to determine the angle that makes this configuration optimal, α was increased from $\alpha = 0^o$ to $\alpha = 180^o$ and the figures of merit were evaluated. The result is presented in Figure 4.4.
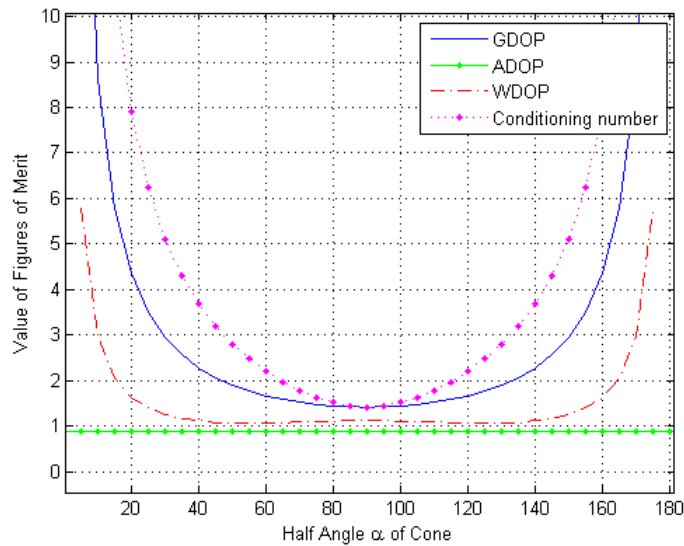
Figure 4.4: Figures of Merit for Cone with Four IMUs Equally Distributed

By inspection of the previous figure, one could infer that the minimum occurs at $\alpha = 90^o$, which would tell us that the IMUs should be on the same plane. The minimum value of GDOP and k occurs at $\alpha = 90^o$, whereas the minimum value of $\dot{\omega}$DOP occurs at $\alpha = 55^o$ and at $\alpha = 125^o$. The values for each angle are summarized in Table 4.3.

21

Table 4.3: Minimum Figures of Merit for four Equally distributed IMUs on a Cone

$\alpha(deg)$	J	$\tilde{J}$	k	GDOP	$\dot{\omega}$DOP	aDOP
90	64	0	**1.4142**	**1.4142**	1.1180	0.8660
55/125	64	0	2.4685	1.7616	**1.0607**	0.8660

The values in bold in Table 4.3 represent the minimum value for that specific angle. If the values when $\alpha = 90^o$ are compared to that of the ones presented in Table 4.1 it will be seen that they are the same, as expected.

4.1.3 Three IMUs on a Cone and one on the Z axis

In this configuration, three IMUs are equally spaced along the surface of a cone and a fourth one is placed on the z axis. Figure 4.5 shows $\alpha = 70^o$ used in the **R** and **D** matrices with $\beta = 60^o$.
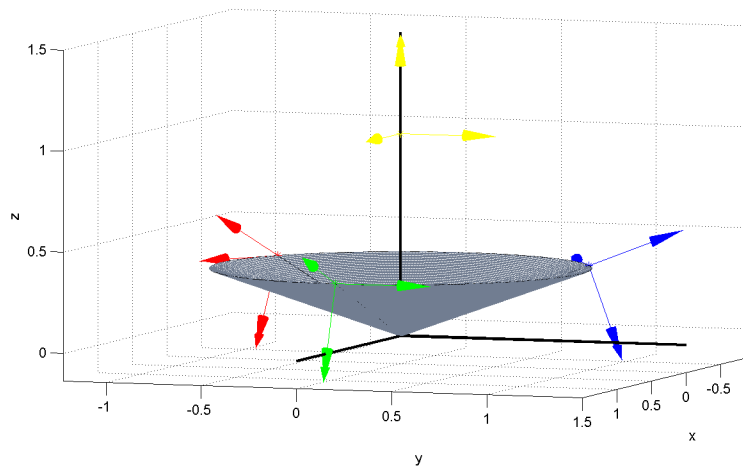

Figure 4.5: Three IMUs on a Cone and One on the Z Axis

22

$$\mathbf{R} = \begin{bmatrix} 0 & 0 & 1 \\ 0 & 0 & 1 \\ 0 & 0 & 1 \\ \sin\alpha & 0 & \cos\alpha \\ \sin\alpha & 0 & \cos\alpha \\ \sin\alpha & 0 & \cos\alpha \\ \sin\alpha\cos\beta & \sin\alpha\sin\beta & \cos\alpha \\ \sin\alpha\cos\beta & \sin\alpha\sin\beta & \cos\alpha \\ \sin\alpha\cos\beta & \sin\alpha\sin\beta & \cos\alpha \\ \sin\alpha\cos 2\beta & \sin\alpha\sin 2\beta & \cos\alpha \\ \sin\alpha\cos 2\beta & \sin\alpha\sin 2\beta & \cos\alpha \\ \sin\alpha\cos 2\beta & \sin\alpha\sin 2\beta & \cos\alpha \end{bmatrix} \quad \mathbf{D} = \begin{bmatrix} 1 & 0 & 0 \\ 0 & 1 & 0 \\ 0 & 0 & 1 \\ \cos\alpha & 0 & -\sin\alpha \\ 0 & 1 & 0 \\ \sin\alpha & 0 & \cos\alpha \\ \frac{1}{2}\cos\alpha & \frac{\sqrt{3}}{2}\cos\alpha & -\sin\alpha \\ -\frac{\sqrt{3}}{2} & \frac{1}{2} & 0 \\ \frac{1}{2}\sin\alpha & \frac{\sqrt{3}}{2}\sin\alpha & \cos\alpha \\ -\frac{1}{2}\cos\alpha & \frac{\sqrt{3}}{2}\cos\alpha & -\sin\alpha \\ -\frac{\sqrt{3}}{2} & -\frac{1}{2} & 0 \\ -\frac{1}{2}\sin\alpha & \frac{\sqrt{3}}{2}\sin\alpha & \cos\alpha \end{bmatrix}$$

$$(4.3)$$

Again the optimum value of α is needed, therefore the different figures of merit are plotted varying the angle from $\alpha = 0^o$ to $\alpha = 180^o$, obtaining Figure 4.6.
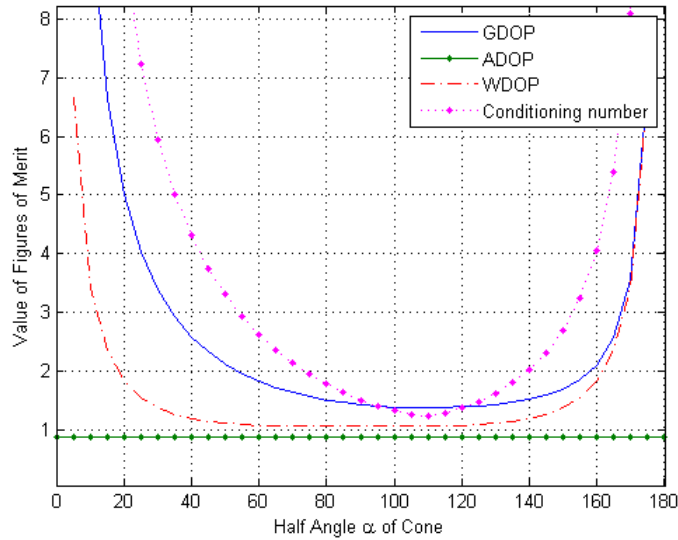
Figure 4.6: Figures of Merit Cone with IMU on z-axis

Figure 4.6 shows how the condition number is shifted to the right. The minimum for the GDOP, $\dot\omega$DOP, and k is at $\alpha = 110^o$. Since this configuration is symmetrical with respect to the vertical, $\dot\omega$DOP shows two minimums, the second one being at $\alpha = 70^o$, as shown in Table 4.4.

Table 4.4: Minimum Figures of Merit for Cone with IMU on Z axis

$\alpha(deg)$	J	$\tilde{J}$	k	GDOP	$\dot\omega$DOP	aDOP
70	64	0	2.1294	1.6283	**1.0607**	0.8660
110	64	0	**1.2289**	**1.3693**	**1.0607**	0.8660

It is evident that in order to get better results, symmetrical configurations should be constructed. Figure 4.7 shows the configurations for $\alpha = 70^o$ and $\alpha = 110^o$.

(a) $\alpha = 70$ (b) $\alpha = 110$
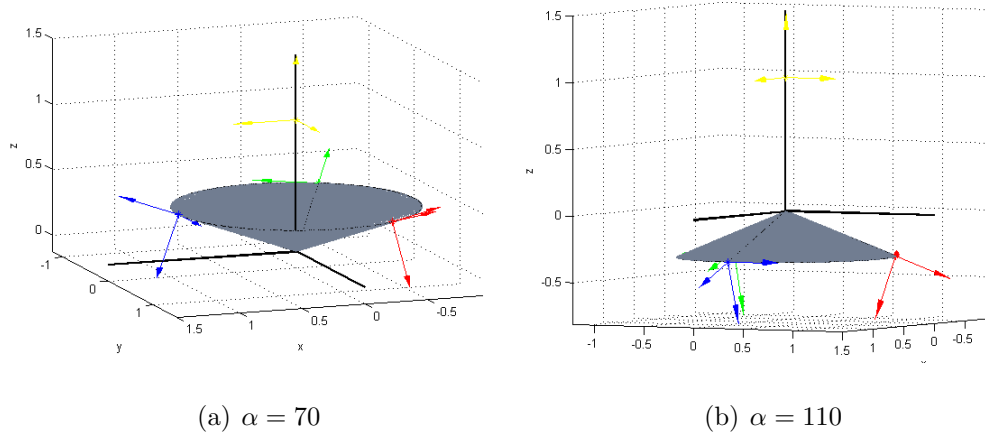
Figure 4.7: Optimal Configurations for Cone with an IMU on the z-xis

4.1.4   Three IMUs on a Cone and one at the Origin

This configurations is very similar to the one in Section 4.1.3. The difference is that instead of having the fourth IMU on the z-axis, it is located at the origin. The **D** matrix is the same as before. The **R** changes in the first three rows since the position of this IMU is zero. The configuration is illustrated in Figure 4.8.
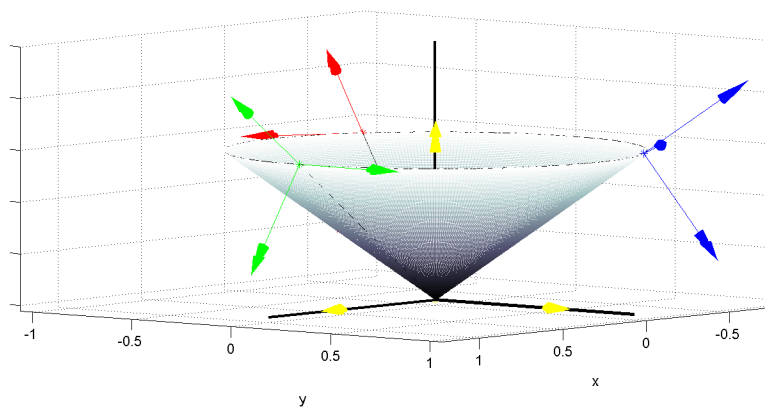
Figure 4.8: Three IMUs on Cone and One at the Origin

$$\mathbf{R} = \begin{bmatrix} 0 & 0 & 0 \\ 0 & 0 & 0 \\ 0 & 0 & 0 \\ \sin\alpha & 0 & \cos\alpha \\ \sin\alpha & 0 & \cos\alpha \\ \sin\alpha & 0 & \cos\alpha \\ \sin\alpha\cos\beta & \sin\alpha\sin\beta & \cos\alpha \\ \sin\alpha\cos\beta & \sin\alpha\sin\beta & \cos\alpha \\ \sin\alpha\cos\beta & \sin\alpha\sin\beta & \cos\alpha \\ \sin\alpha\cos2\beta & \sin\alpha\sin2\beta & \cos\alpha \\ \sin\alpha\cos2\beta & \sin\alpha\sin2\beta & \cos\alpha \\ \sin\alpha\cos2\beta & \sin\alpha\sin2\beta & \cos\alpha \end{bmatrix} \quad \mathbf{D} = \begin{bmatrix} 1 & 0 & 0 \\ 0 & 1 & 0 \\ 0 & 0 & 1 \\ \cos\alpha & 0 & -\sin\alpha \\ 0 & 1 & 0 \\ \sin\alpha & 0 & \cos\alpha \\ \frac{1}{2}\cos\alpha & \frac{\sqrt{3}}{2}\cos\alpha & -\sin\alpha \\ -\frac{\sqrt{3}}{2} & \frac{1}{2} & 0 \\ \frac{1}{2}\sin\alpha & \frac{\sqrt{3}}{2}\sin\alpha & \cos\alpha \\ -\frac{1}{2}\cos\alpha & \frac{\sqrt{3}}{2}\cos\alpha & -\sin\alpha \\ -\frac{\sqrt{3}}{2} & -\frac{1}{2} & 0 \\ -\frac{1}{2}\sin\alpha & \frac{\sqrt{3}}{2}\sin\alpha & \cos\alpha \end{bmatrix}$$

$$(4.4)$$

Evaluating the figures of merit for this configuration presents minimums at $\alpha = 90^o$ and at 55 and $\alpha = 125^o$ as shown in Figure 4.9
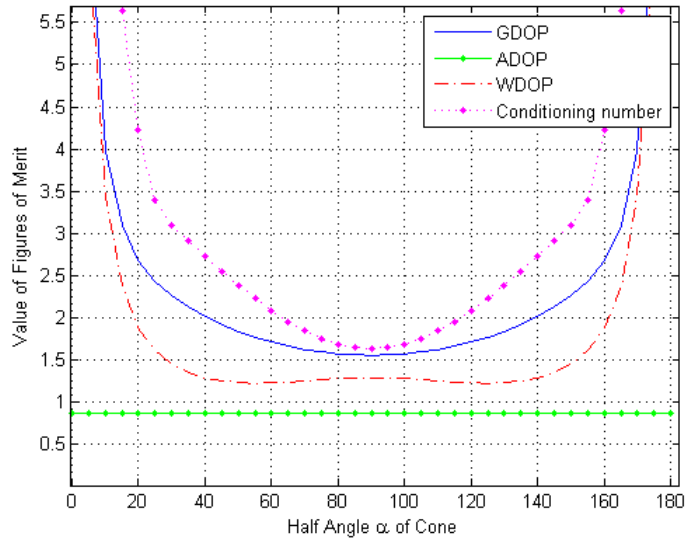
Figure 4.9: Figures of Merit Cone with IMU at Origin

Table 4.5: Minimum Figures of Merit for Cone with IMU at Origin

$\alpha(deg)$	J	$\tilde{J}$	k	GDOP	$\dot{\omega}$DOP	aDOP
90	64	0	**1.6330**	**1.5546**	1.2910	0.8660
55/125	64	0	2.2281	1.7714	**1.2248**	0.8660

One might think that when have $\alpha = 90^o$, the values should be equal to that of the IMUs on a square. The values are different since one of the IMUs, in this case, is at the origin and therefore confirms that the symmetry is important. Figure 4.10 show the cases for $\alpha = 90^o$ and $\alpha = 55^o$.

(a) $\alpha = 90$ (b) $\alpha = 55$
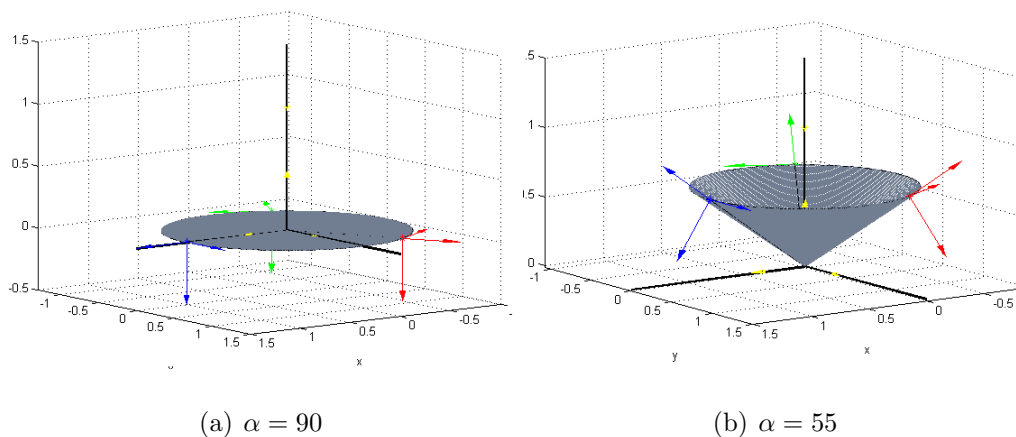
Figure 4.10: Optimal Configurations for Cone with IMU at Origin

Even though Figure 4.10(a) is on a plane, the figures of merit are larger than that of the square presented in Section 4.1.1. This is due to the geometry.

4.1.5 Triangle

This configurations intends to show how the symmetry affects the figures of merit. We will have the same four IMUs as in Section 4.1.1 but now

27

they will be placed asymmetrical in a triangular configuration.
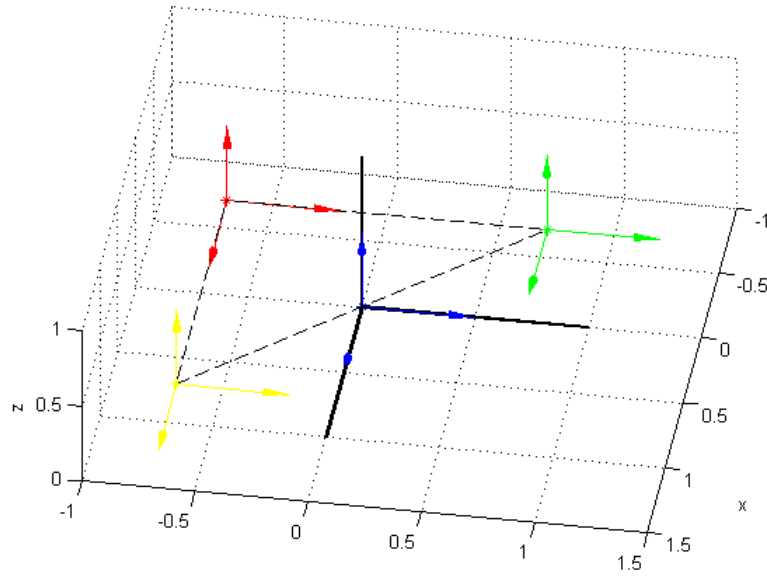
Figure 4.11: Triangle Configuration

$$\mathbf{R} = \frac{1}{\sqrt{2}} \begin{bmatrix} 0 & 0 & 0 \\ 0 & 0 & 0 \\ 0 & 0 & 0 \\ -1 & 1 & 0 \\ -1 & 1 & 0 \\ -1 & 1 & 0 \\ -1 & -1 & 0 \\ -1 & -1 & 0 \\ -1 & -1 & 0 \\ 1 & -1 & 0 \\ 1 & -1 & 0 \\ 1 & -1 & 0 \end{bmatrix} \quad \mathbf{D} = \begin{bmatrix} 1 & 0 & 0 \\ 0 & 1 & 0 \\ 0 & 0 & 1 \\ 1 & 0 & 0 \\ 0 & 1 & 0 \\ 0 & 0 & 1 \\ 1 & 0 & 0 \\ 0 & 1 & 0 \\ 0 & 0 & 1 \\ 1 & 0 & 0 \\ 0 & 1 & 0 \\ 0 & 0 & 1 \end{bmatrix} \qquad (4.5)$$

The values obtained by the figures of merit are small but not as small as the square, as illustrated in Table 4.6

28

Table 4.6: Figures of Merit for a Square and Triangle

	J	$\tilde{J}$	k	GDOP	$\dot{\omega}$DOP	aDOP
Square	64	0	1.4142	1.4142	1.1180	0.8660
Triangle	64	0	2.5736	1.7473	1.3540	0.8660

With this we can conclude that symmetry is important when the IMUs are placed on the same plane.

4.1.6 Summary of Results with Configuration of Four IMUs

Table 4.7 presents a summary of the configurations that use four IMUs. Table 4.7 shows the best configurations marked with a star and bold and the second best only bold. The cone with one IMU on the z-axis shows the most optimal values of GDOP, $\dot{\omega}$DOP, and k. This is due to the fact that the configuration is not only symmetrical with respect to the xy-plane, but is also symmetrical with respect to the z-axis, creating more symmetry than if they were all placed on the xy-plane. An example of all the sensors on the plane is to place them on the vertices of a square, which gives the next best figures of merit. Another configuration that was tested is placing the IMUs on the surface of a cone, at the same z distance from the origin. The half angle was varied from $0 \leq \alpha \leq 90^o$ and gave optimal results at $\alpha = 90^o$, which coincides with placing the IMUs on a square on the plane. Therefore, it is better to place the IMUs on the plane than on the surface of a cone. Lastly, three IMUs were placed on the vertices of a triangle and the fourth one at the origin. This configuration gave large results in the figures of merit. Even though it is a configuration on the xy-plane, it not symmetric about both axis, as is the

29

square configuration. Therefore, anytime that four IMUs want to be placed on the plane, it is best to produce a symmetrical configuration. In Table 4.7, note that the values of aDOP remain constant for all configurations since they only depend on the number of sensors used.

Table 4.7: Comparison of Figures for Configurations of Four IMUs. Note, $^+$ indicates a cone configuration.

	α	J	$\tilde{J}$	k	GDOP	$\dot{\omega}$DOP	aDOP
Square in Plane	-	64	0	**1.4142**	**1.4142**	1.1180	0.8660
4 Equally Spaced$^+$	54	64	0	2.4853	1.7682	1.0607	0.8660
4 Equally Spaced$^+$	90	64	0	1.4142	1.4142	1.1180	0.8660
4 Equally Spaced$^+$	55/125	64	0	2.4685	1.7616	1.0607	0.8660
One @Z Axis$^+$	70	64	0	2.1294	1.6283	1.0607	0.8660
One @Z Axis$^+$	110	64	0	**1.2289***	**1.3693***	**1.0607***	0.8660
One @Origin$^+$	90	64	0	1.6330	1.5546	1.2910	0.8660
One @Origin$^+$	55/125	64	0	2.2281	1.7714	1.2248	0.8660
Triangle	-	64	0	2.5736	1.7473	1.3540	0.8660

4.2 Configurations with Eight IMUs

This section presents configurations with eight IMUs. A cube, a unit circle, a cone with eight IMUs equally distributed, two cones with four IMUs each, and an octahedron are presented.

4.2.1 Cube

The cube configuration has one IMU in each of its vertices. The position matrix in Eq. (4.6) is

$$
\mathbf{R} = \frac{1}{\sqrt{3}}
\begin{bmatrix}
1 & 1 & 1 \\
1 & 1 & 1 \\
1 & 1 & 1 \\
1 & 1 & -1 \\
1 & 1 & -1 \\
1 & 1 & -1 \\
1 & -1 & -1 \\
1 & -1 & -1 \\
1 & -1 & -1 \\
1 & -1 & 1 \\
1 & -1 & 1 \\
1 & -1 & 1 \\
-1 & 1 & 1 \\
-1 & 1 & 1 \\
-1 & 1 & 1 \\
-1 & 1 & -1 \\
-1 & 1 & -1 \\
-1 & 1 & -1 \\
-1 & -1 & -1 \\
-1 & -1 & -1 \\
-1 & -1 & -1 \\
-1 & -1 & 1 \\
-1 & -1 & 1 \\
-1 & -1 & 1
\end{bmatrix}
\tag{4.6}
$$

Two different orientations were tested and gave the same results. For this reason, the orientation matrix $\mathbf{D}$ is not shown. The orientations are the cube with identity orientations (Figure 4.12) and the cube with orientations following the edges (Figure 4.13).
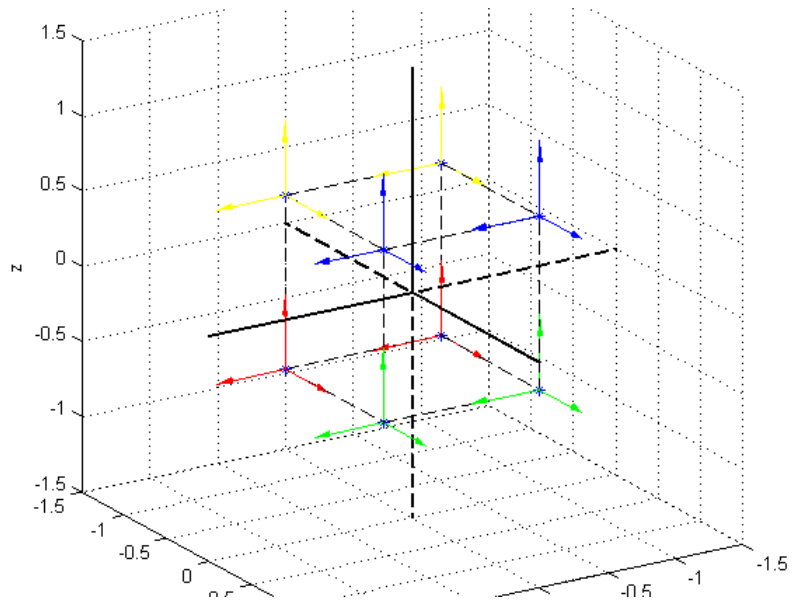
Figure 4.12: Cube with Identity Orientations

The second configuration in Figure 4.13 has the sensing axis pointing to each of the sides of the cube. Table 4.8 shows that the value of GDOP and $\dot{\omega}$ are relatively small. Later it will be seen that this configuration gets the smallest values in the figures of merit.
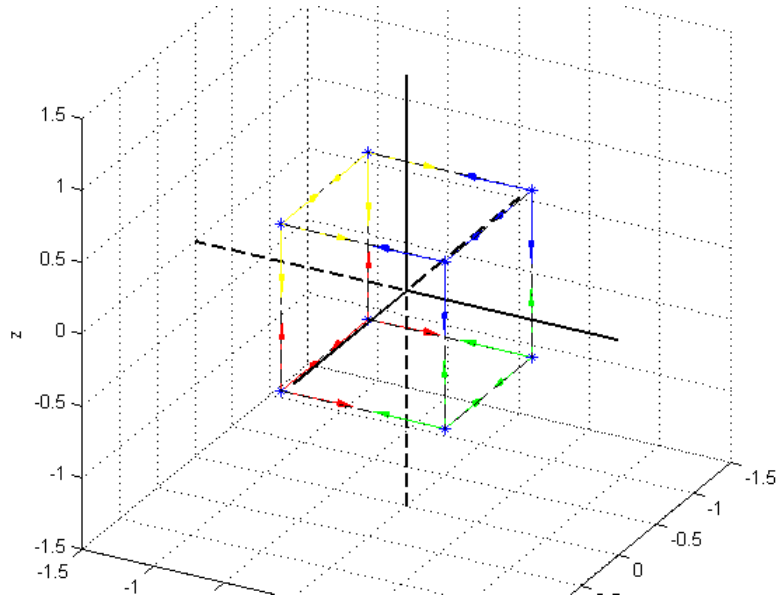
Figure 4.13: Cube with Inside Orientations

Table 4.8: Figures of Merit for a Cube

	J	$\tilde{J}$	k	GDOP	$\dot{\omega}$DOP	aDOP
Cube	512	0	1.2247	0.9682	0.75	0.6124

4.2.2 Unit Circle

This configuration shows eight IMUs equally distributed along the circumference of a unit circle. Two different orientations are presented in Figure 4.14 and 4.15.

Figure 4.14: Unit Circle with Identity Direction

Figure 4.15: Unit Circle with Rotating Direction

34

The **R** matrix in Eq.(4.7) describes their position.

$$
\mathbf{R} = \frac{1}{\sqrt{2}}
\begin{bmatrix}
1 & 0 & 0 \\
1 & 0 & 0 \\
1 & 0 & 0 \\
\frac{1}{\sqrt{2}} & \frac{1}{\sqrt{2}} & 0 \\
\frac{1}{\sqrt{2}} & \frac{1}{\sqrt{2}} & 0 \\
\frac{1}{\sqrt{2}} & \frac{1}{\sqrt{2}} & 0 \\
0 & 1 & 0 \\
0 & 1 & 0 \\
0 & 1 & 0 \\
-\frac{1}{\sqrt{2}} & \frac{1}{\sqrt{2}} & 0 \\
-\frac{1}{\sqrt{2}} & \frac{1}{\sqrt{2}} & 0 \\
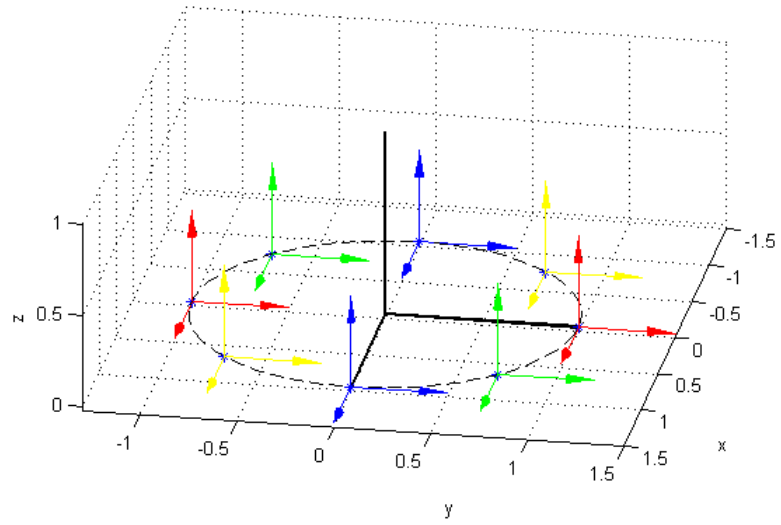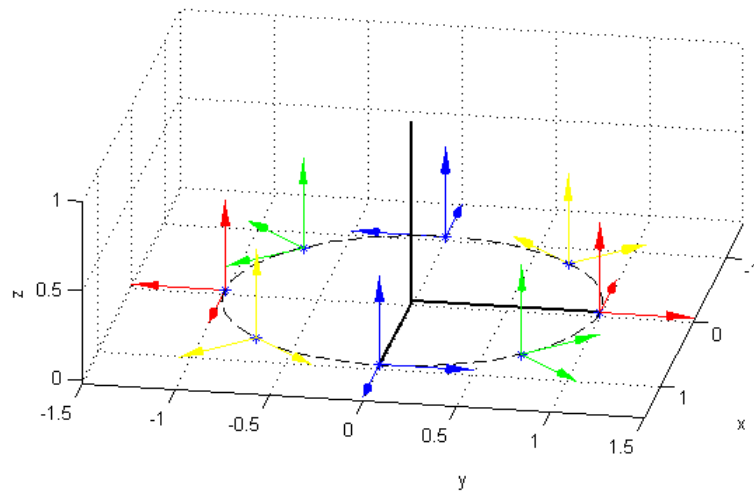-\frac{1}{\sqrt{2}} & \frac{1}{\sqrt{2}} & 0 \\
-1 & 0 & 0 \\
-1 & 0 & 0 \\
-1 & 0 & 0 \\
-\frac{1}{\sqrt{2}} & -\frac{1}{\sqrt{2}} & 0 \\
-\frac{1}{\sqrt{2}} & -\frac{1}{\sqrt{2}} & 0 \\
-\frac{1}{\sqrt{2}} & -\frac{1}{\sqrt{2}} & 0 \\
0 & -1 & 0 \\
0 & -1 & 0 \\
0 & -1 & 0 \\
\frac{1}{\sqrt{2}} & -\frac{1}{\sqrt{2}} & 0 \\
\frac{1}{\sqrt{2}} & -\frac{1}{\sqrt{2}} & 0 \\
\frac{1}{\sqrt{2}} & -\frac{1}{\sqrt{2}} & 0
\end{bmatrix}
\tag{4.7}
$$

Again, the results for both orientations are the same, which tells us that the figures of merit are unchanged by the orientation and are more ruled by the position of the sensors. Table 4.9 shows the figures of merit for the unit circle. All three values of condition number k, GDOP, and $\dot{\omega}$DOP are larger that the ones obtained for the cube.

Table 4.9: Figures of Merit for a Unit Circle

	J	$\tilde{J}$	k	GDOP	$\dot{\omega}$DOP	aDOP
Unit Circle	512	0	1.4142	1.000	0.7906	0.6124

4.2.3   Cone With Eight Equally Distributed IMUs

This configuration has the eight IMUs distributed along the surface of the cone, as illustrated in Figure 4.16. Different α angles for the cone were tested.
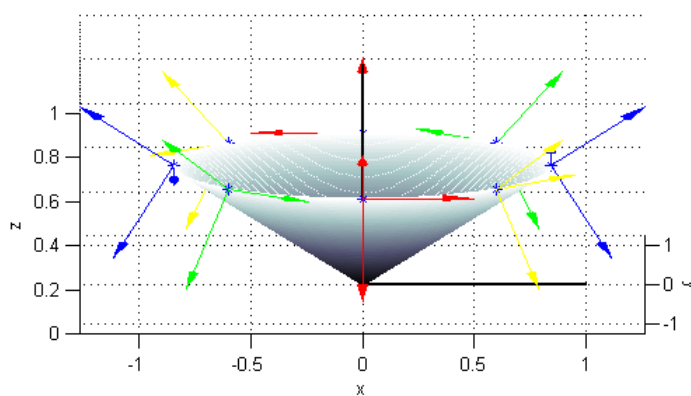

Figure 4.16: Cone with $\alpha = 55$

The **R** matrix in Eq. (4.8) describes their position of the IMUs.

$$\mathbf{R} = \begin{bmatrix}
\sin\alpha & 0 & \cos\alpha \\
\sin\alpha & 0 & \cos\alpha \\
\sin\alpha & 0 & \cos\alpha \\
\frac{1}{\sqrt{2}}\sin\alpha & \frac{1}{\sqrt{2}}\sin\alpha & \cos\alpha \\
\frac{1}{\sqrt{2}}\sin\alpha & \frac{1}{\sqrt{2}}\sin\alpha & \cos\alpha \\
\frac{1}{\sqrt{2}}\sin\alpha & \frac{1}{\sqrt{2}}\sin\alpha & \cos\alpha \\
0 & \sin\alpha & \cos\alpha \\
0 & \sin\alpha & \cos\alpha \\
0 & \sin\alpha & \cos\alpha \\
-\frac{1}{\sqrt{2}}\sin\alpha & \frac{1}{\sqrt{2}}\sin\alpha & \cos\alpha \\
-\frac{1}{\sqrt{2}}\sin\alpha & \frac{1}{\sqrt{2}}\sin\alpha & \cos\alpha \\
-\frac{1}{\sqrt{2}}\sin\alpha & \frac{1}{\sqrt{2}}\sin\alpha & \cos\alpha \\
-\sin\alpha & 0 & \cos\alpha \\
-\sin\alpha & 0 & \cos\alpha \\
-\sin\alpha & 0 & \cos\alpha \\
-\frac{1}{\sqrt{2}}\sin\alpha & -\frac{1}{\sqrt{2}}\sin\alpha & \cos\alpha \\
-\frac{1}{\sqrt{2}}\sin\alpha & -\frac{1}{\sqrt{2}}\sin\alpha & \cos\alpha \\
-\frac{1}{\sqrt{2}}\sin\alpha & -\frac{1}{\sqrt{2}}\sin\alpha & \cos\alpha \\
0 & -\sin\alpha & \cos\alpha \\
0 & -\sin\alpha & \cos\alpha \\
0 & -\sin\alpha & \cos\alpha \\
\frac{1}{\sqrt{2}}\sin\alpha & -\frac{1}{\sqrt{2}}\sin\alpha & \cos\alpha \\
\frac{1}{\sqrt{2}}\sin\alpha & -\frac{1}{\sqrt{2}}\sin\alpha & \cos\alpha \\
\frac{1}{\sqrt{2}}\sin\alpha & -\frac{1}{\sqrt{2}}\sin\alpha & \cos\alpha
\end{bmatrix} \tag{4.8}$$

The angle α was changed from 0° to 180° yielding the figures of merit shown in Figure 4.17.

37
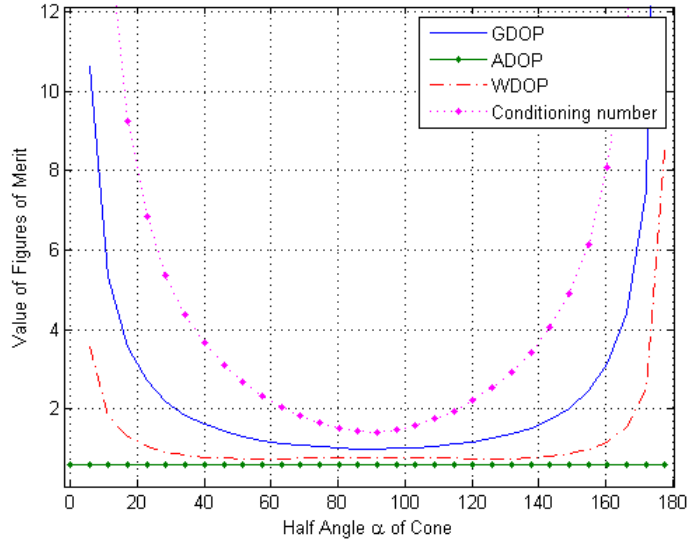
Figure 4.17: Figures of Merit Cone with Eight IMU

The minimum of GDOP and the condition number k occurs at $\alpha = 90^o$. For $\dot{\omega}$DOP, the minimum is at $\alpha = 125^o$ and at $\alpha = 55^o$. The values for $\alpha = 90^o$ are very close to that of the unit circle of the previous section. This is due to the fact the IMUs form the same configurations. Table 4.10 shows in bold the smallest values obtained. The values of k and GDOP are larger that those of the cube. The value of $\dot{\omega}$ at $\alpha = 55$ is close to that of the cube.

Table 4.10: Minimum Figures of Merit for Cone with Eight Equally distributed IMUs

$\alpha(deg)$	J	$\tilde{J}$	k	GDOP	$\dot{\omega}$DOP	aDOP
90	512	0	**1.4142**	**1.0005**	0.7904	0.6124
55/125	512	0	2.5317	1.2634	**0.7501**	0.6124

4.2.4 Two Cones With Four IMUs Each

This configuration shows two identical cones, joined by their tip, as illustrated in Figure 4.18.

Figure 4.18: Cone with $\alpha = 55$

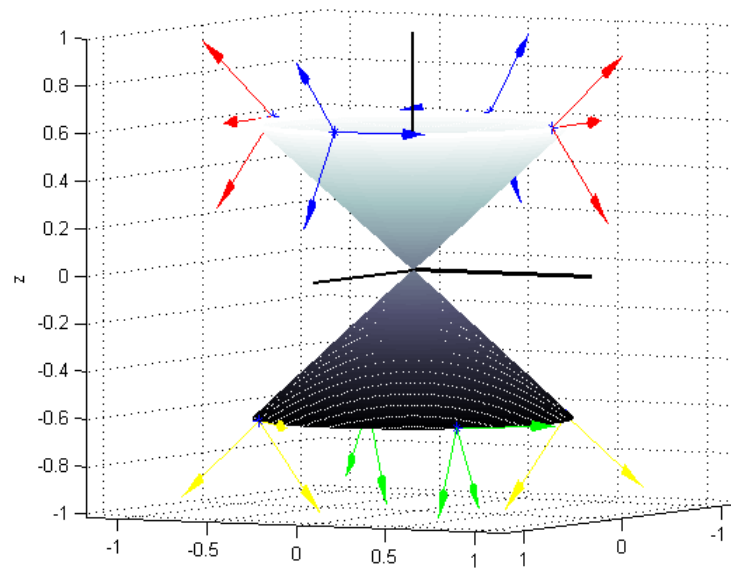The $\mathbf{R}$ matrix describes the IMU position with respect to the angle α.

$$\mathbf{R} = \begin{bmatrix} \sin\alpha & 0 & \cos\alpha \\ \sin\alpha & 0 & \cos\alpha \\ \sin\alpha & 0 & \cos\alpha \\ \frac{1}{\sqrt{2}}\sin\alpha & \frac{1}{\sqrt{2}}\sin\alpha & -\cos\alpha \\ \frac{1}{\sqrt{2}}\sin\alpha & \frac{1}{\sqrt{2}}\sin\alpha & -\cos\alpha \\ \frac{1}{\sqrt{2}}\sin\alpha & \frac{1}{\sqrt{2}}\sin\alpha & -\cos\alpha \\ 0 & \sin\alpha & \cos\alpha \\ 0 & \sin\alpha & \cos\alpha \\ 0 & \sin\alpha & \cos\alpha \\ -\frac{1}{\sqrt{2}}\sin\alpha & \frac{1}{\sqrt{2}}\sin\alpha & -\cos\alpha \\ -\frac{1}{\sqrt{2}}\sin\alpha & \frac{1}{\sqrt{2}}\sin\alpha & -\cos\alpha \\ -\frac{1}{\sqrt{2}}\sin\alpha & \frac{1}{\sqrt{2}}\sin\alpha & -\cos\alpha \\ -\sin\alpha & 0 & \cos\alpha \\ -\sin\alpha & 0 & \cos\alpha \\ -\sin\alpha & 0 & \cos\alpha \\ -\frac{1}{\sqrt{2}}\sin\alpha & -\frac{1}{\sqrt{2}}\sin\alpha & -\cos\alpha \\ -\frac{1}{\sqrt{2}}\sin\alpha & -\frac{1}{\sqrt{2}}\sin\alpha & -\cos\alpha \\ -\frac{1}{\sqrt{2}}\sin\alpha & -\frac{1}{\sqrt{2}}\sin\alpha & -\cos\alpha \\ 0 & -\sin\alpha & \cos\alpha \\ 0 & -\sin\alpha & \cos\alpha \\ 0 & -\sin\alpha & \cos\alpha \\ \frac{1}{\sqrt{2}}\sin\alpha & -\frac{1}{\sqrt{2}}\sin\alpha & -\cos\alpha \\ \frac{1}{\sqrt{2}}\sin\alpha & -\frac{1}{\sqrt{2}}\sin\alpha & -\cos\alpha \\ \frac{1}{\sqrt{2}}\sin\alpha & -\frac{1}{\sqrt{2}}\sin\alpha & -\cos\alpha \end{bmatrix} \tag{4.9}$$

The angle α was also changed from $\alpha = 0^o$ to $\alpha = 180^o$ yielding Figure 4.19.
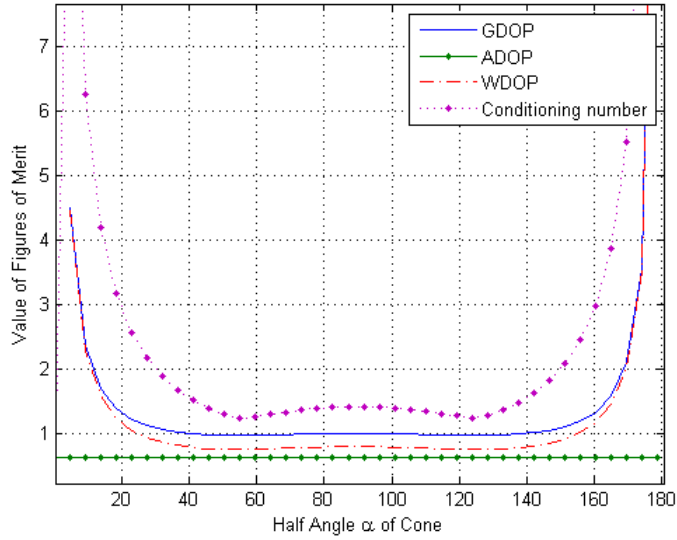
Figure 4.19: Figures of Merit for two Cones with Eight IMUs

The minimums for GDOP, k, and $\dot{\omega}$DOP occur at $\alpha = 125^o$ or at $\alpha = 55^o$. The values are presented in Table 4.11. Also the values at $\alpha = 45^o$ are presented for a later comparison.

Table 4.11: Minimum Figures of Merit for Two Cones with Four Equally distributed IMUs

$\alpha(deg)$	J	$\tilde{J}$	k	GDOP	$\dot{\omega}$DOP	aDOP
45	512	0	1.4142	0.9789	0.7638	0.6124
55/125	512	0	**1.2268**	**0.9683**	**0.7500**	0.6124

The two cone configurations at angles of $\alpha = 55^0$ and $\alpha = 125^o$ give the same results as the cube configuration. In fact, at that angle, the configurations are the identical since their position in space is the same.

41

4.2.5 Octahedron

This configuration has eight IMUs placed on each of the edges of an octahedron, as illustrated in Figure 4.20. The α angle is measured from the xy-plane to the positive z-axis.

Figure 4.20: Octahedron with $\alpha = 45$

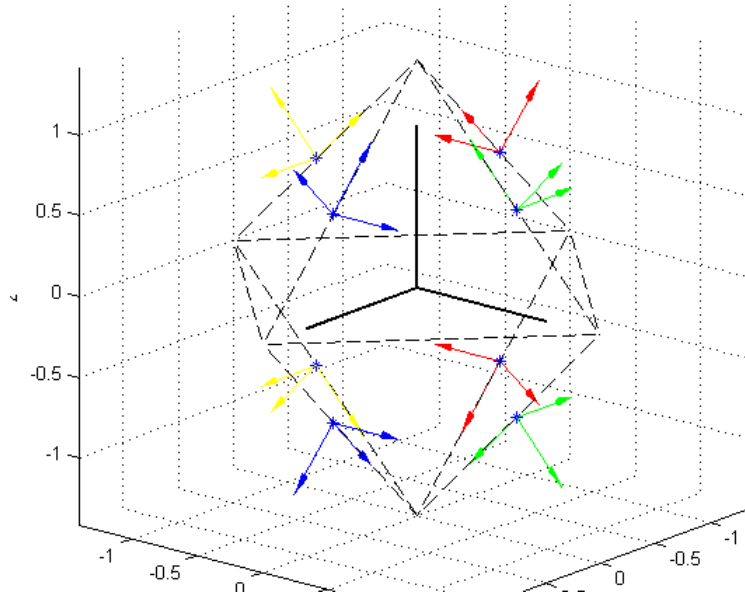The **R** matrix in Eq. (4.10)describes the position of the IMUs as a function of the angle α.

$$\mathbf{R} = \begin{bmatrix} \cos\alpha & 0 & \sin\alpha \\ \cos\alpha & 0 & \sin\alpha \\ \cos\alpha & 0 & \sin\alpha \\ 0 & \cos\alpha & \sin\alpha \\ 0 & \cos\alpha & \sin\alpha \\ 0 & \cos\alpha & \sin\alpha \\ -\cos\alpha & \sin\alpha & \sin\alpha \\ -\cos\alpha & \sin\alpha & \sin\alpha \\ -\cos\alpha & \sin\alpha & \sin\alpha \\ 0 & -\cos\alpha & \sin\alpha \\ 0 & -\cos\alpha & \sin\alpha \\ 0 & -\cos\alpha & \sin\alpha \\ \cos\alpha & 0 & -\sin\alpha \\ \cos\alpha & 0 & -\sin\alpha \\ \cos\alpha & 0 & -\sin\alpha \\ 0 & \cos\alpha & -\sin\alpha \\ 0 & \cos\alpha & -\sin\alpha \\ 0 & \cos\alpha & -\sin\alpha \\ -\cos\alpha & \sin\alpha & -\sin\alpha \\ -\cos\alpha & \sin\alpha & -\sin\alpha \\ -\cos\alpha & \sin\alpha & -\sin\alpha \\ 0 & -\cos\alpha & \sin\alpha \\ 0 & -\cos\alpha & \sin\alpha \\ 0 & -\cos\alpha & \sin\alpha \end{bmatrix} \tag{4.10}$$

The angle α was varied from $\alpha = 0^o$ to $\alpha = 180^o$ as shown in Figure 4.21, yielding the following figure of merit plot shown in Figure 4.22.

(a) $\alpha = 0$ (b) $\alpha = 90$
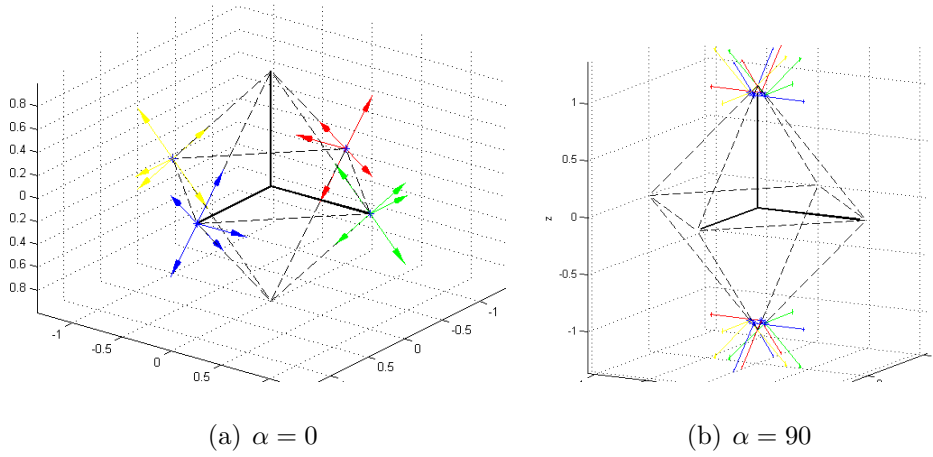
Figure 4.21: Configurations for Octahedron
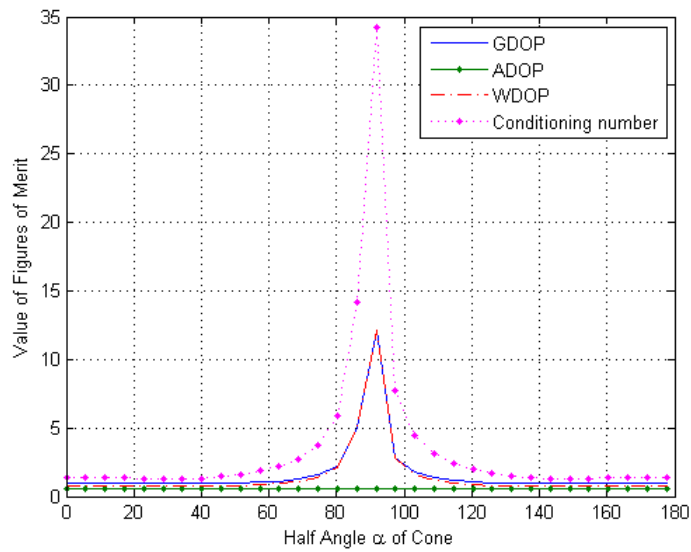
Figure 4.22: Figures of Merit for Octahedron

The minimum values for GDOP, k, and $\dot{\omega}$DOP occurs at $\alpha = 34.4^o$. The values are presented in Table 4.12. When $\alpha = 90^o$ we observe that all the figures of

merit values grow exponentially. This behavior is because at that angle, the geometrical configuration is equivalent to having four IMUs stacked at one vertex, and it is not a good idea to have them all together. Also the values at $\alpha = 45^o$ are presented in Table 4.12.

Table 4.12: Minimum Figures of Merit for Octahedron

$\alpha(deg)$	J	$\tilde{J}$	k	GDOP	$\dot{\omega}$DOP	aDOP
45	512	0	1.4142	0.9789	0.7638	0.6124
34.4	512	0	**1.2315**	**0.9683**	**0.7501**	0.6124

When the angle is $\alpha = 34.4^o$, the values are close to that of the cube, and as seen in Figure 4.23, indeed, they are practically the same configuration.
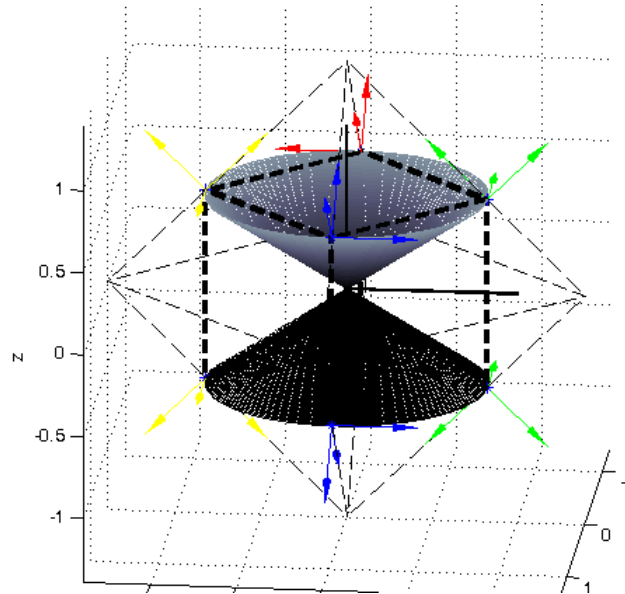
Figure 4.23: Equivalent Octahedron, Cube, and Two Cones

When $\alpha = 45^o$, the values are the same as the ones obtained in the two cone configuration at that same angle. In Figure 4.24, it was noticed that the two cone configuration and the octahedron are equivalent and the only difference is how we measure the angle α. The figures of merit confirm that the octahedron at $90 - \alpha$ gives the same values as for the two cones at an angle α, as shown in Figure 4.25.
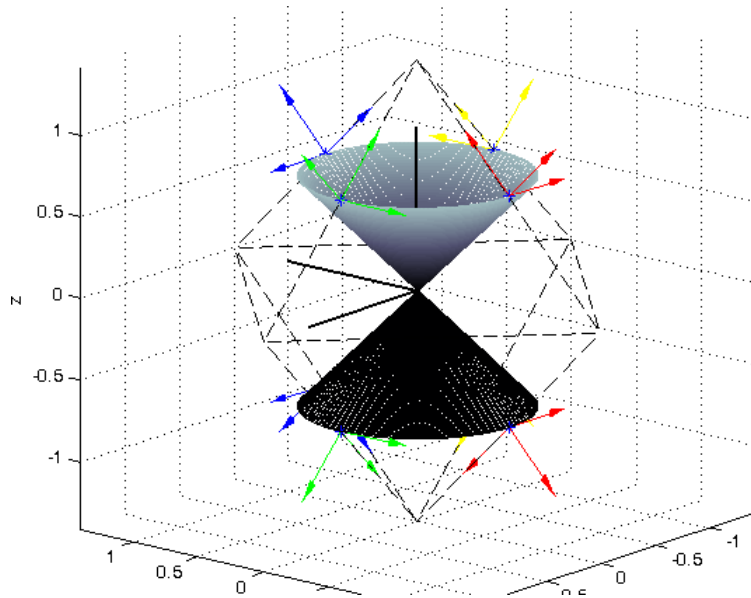
Figure 4.24: Equivalent Octahedron and Two Cones
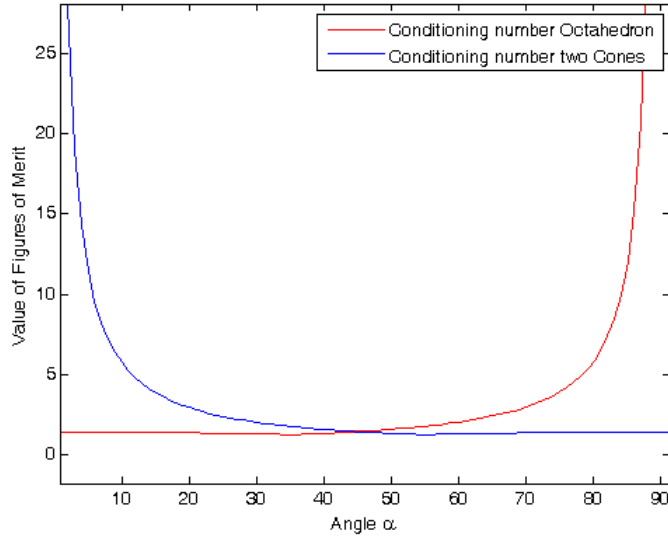
Figure 4.25: Figures of Merit for Octahedron and Two Cones

4.2.6 Summary of Results with Configurations of Eight IMUs

In Table 4.13, we present the summary of the results of the configurations using eight IMUs. Table 4.13 shows that the minimum figure of merit values are obtained with the cube configuration (marked with * and bold). The second best configuration is the octahedron at $\alpha = 34.4^o$, but this is the equivalent configuration to that of the cube, as was explained in Section 4.2.5. Also, placing the eight sensors on an octahedron is equivalent to placing them on the two-cone configuration. Therefore, an octahedron at $\alpha = 34.4^o$ is equivalent to the two-cone at $\alpha = 55.6^o$, which is another optimal configuration. The next best configuration is the unit circle on the plane, which is followed by a single cone. Just as in four IMUs configuration, the equally spaced sensors

47

on a cone show the best results when $\alpha = 90^o$, which confirms that in-plane configurations are preferred to single cone configurations.

Table 4.13: Figures of Merit for Configurations of Eight IMUs

	α	J	$\tilde{J}$	k	GDOP	$\dot{\omega}$DOP	aDOP
Cube	-	512	0	1.2247*	0.9682*	0.7500*	0.6124
Unit Circle	0	512	0	1.4142	1.0000	0.7906	0.6124
One Cone	90	512	0	1.4142	1.0005	0.7904	0.6124
One Cone	55/125	512	0	2.5317	1.2634	0.7501	0.6124
Two Cones	45	512	0	1.4142	0.9789	0.7638	0.6124
Two Cones	55/125	512	0	1.2268	0.9683	0.7500	0.6124
Octahedron	45	512	0	1.4142	0.9789	0.7638	0.6124
Octahedron	34.4	512	0	1.2315	0.9683	0.7501	0.6124

As seen in Table 4.13, the figures of merit of the cube are smaller than those for the unit circle on the plane. This result is due to the fact that the cube is symmetric in all the directions with respect to the origin, while the unit circle is symmetric in just the xy plane.

48

Chapter 5

Conclusions

5.1 Research Summary

This research explored the optimality of different geometrical configurations of redundant IMUs, with the purpose of obtaining improvement in the accuracy of the measurements. These configurations were formed with groups of both four and eight IMUs. The configurations tested were a square, a unit circle, and a triangle, all placed on the plane, and in three-dimensions a single cone, two cones joined by their tip, a cube, and a tetrahedron. These geometries were then compared based on six different figures of merit. Of the six, three are based on the position of either the accelerometers or the gyros, one takes into account the rotational part of the configuration, and the remaining two measure both the rotational part and the position of the sensors.

It was shown that the figures of merit were invariant to the orientation of the sensors. That is, the result of putting an IMU with one of its sensing axis facing down is the same as putting the same sensor facing up. It was also determined that the $aDOP$ figure of merit is closely related to the information matrix approach and only depends on the number of IMUs used and not on the geometrical configuration. That is, the $aDOP$ value is the same for a specific

number of IMUs regardless of the geometry. Two of the figures of merit, GDOP and the condition number k, give a sense of the the optimal geometry, with numerically small values being best for GDOP, and values closer to unity for k. The $\dot{\omega}$DOP, another figure of merit, gives a measure for the rotation arm. The smaller this value, the more spread out a configuration is, and therefore having a longer rotation arm increases the magnitude of the measurement.

For configurations with four IMUs, it was shown that the configuration of a single cone gives high values in the figures of merit if all the IMUs are equally spaced along the surface of the cone, and therefore it is not advised to use this configuration. A better result was found placing them on the edges of a square. However, the best configuration is to place three of the IMUs along the surface of a cone with a half angle $\alpha = 110^o$ and the remaining IMU above on the z-axis. A triangle configuration was also considered, but did not give optimal conditions. This last configuration was tested to prove that, if placing the sensors on the plane, symmetrical configurations will always give optimal conditions.

According to the results of the figures of merit, for configurations with eight IMUs, the cube turned out to be the most optimal configuration. If the cube is compared to the unit circle, it is found that all three values of condition number k, GDOP, and $\dot{\omega}$DOP are smaller for the cube. This result is due to the fact that the cube is symmetric in all the directions with respect to the origin, while the unit circle is symmetric in just the xy-plane. The second best configuration is the octahedron. For an angle $\alpha = 34.4^o$, the values of its

figures of merit are close to that of the cube, meaning that the positions of the IMUs are close to that of the cube. It was noticed that the octahedron and the two cones joined by their tips are equivalent. For the single cone configuration, its minimum is at $\alpha = 90^o$, which is the same as the unit circle, confirming that the in-plane configuration is better than any single cone configuration.

5.2 Future Work

The research presented herein compares theoretically the optimality of placing different number of IMUs in several geometrical configurations. Future work will be focused on confirming the theoretical results with practical implementation. The different optimal configurations found in this report will be constructed and tested in an R/C airplane. These different optimal configurations need to be compared to the outputs of a tactical IMU to see the performance improvement.

Also this research used the measurements of the sensors in the form of a linear system, where least squares can used to solve the system. Further research should be done to integrate the measurements using different methods, such as the Kalman Filter. After the fusion, the error reduction should be evaluated to determine the impact of the geometry on the error.

Bibliography

[1] J.B. Bancroft. Multiple IMU Integration for Vehicular Navigation. *ION GNSS*, 2009.

[2] J.H. Chen, S.C. Lee, and D.B. DeBra. Gyroscope free strapdown inertial measurement unit by six linear accelerometers. *Journal of Guidance, Control, and Dynamics*, 17(2):286–290, 1994.

[3] I. Colomina, M. Giménez, JJ Rosales, M. Wis, A. Gómez, P. Miguelsanz, S. Castelldefels, and S. Madrid. Redundant imus for precise trajectory determination. *International Archives of Photogrammetry, Remote Sensing and Spatial Information Sciences*, 34(Part B):7, 2004.

[4] J. Farrel. *Aided Navigation, GPS with High Rate Sensors*. Mc Graw Hill, 2008.

[5] S. Guerrier. Integration of skew-redundant mems-imu with gps for improved navigation performance. Master's thesis, Ecole Polytechnique Federale de Lausanne, 2008.

[6] S. Guerrier. Improving accuracy with multiple sensors: Study of redundant mems-imu/gps configurations. In *Proceedings of the 22nd International Technical Meeting of The Satellite Division of the Institute of*

Navigation (ION GNSS 2009), pages 3114–3121, Savannah International Convention Center, Savannah, GA, 2009. ION GNSS.

[7] R. Hanson. Using multiple mems imus to form a distributed inertial measurement unit. Master's thesis, Air Force Inst of Tech Wright-Patterson Air Force Base Ohio, School of Engineering and Management, 2005.

[8] J.V. Harrison and E.G. Gai. Evaluating sensor orientations for navigation performance and failure detection. *IEEE Transactions on Aerospace and Electronic Systems*, (6):631–643, 1977.

[9] Yongwhan Lim. Symmetry groups of platonic solids. Technical report, Standford, 2008.

[10] B. Malay. Stellar-aided inertial navigation systems on the surface of mars. Master's thesis, The University of Texas at Austin, 2003.

[11] J.B. McKay and M. Pachter. Geometry optimization for gps navigation. In *Proceedings of the 36th IEEE Conference on Decision and Control*, volume 5, pages 4695–4699. IEEE, 2002.

[12] A.J. Pejsa. Optimum skewed redundant inertial navigators. *AIAA Journal*, 12:899–902, 1974.

[13] A.A. Seemkooei. Comparison of reliability and geometrical strength criteria in geodetic networks. *Journal of geodesy*, 75(4):227–233, 2001.

[14] S. Sukkarieh, P. Gibbens, B. Grocholsky, K. Willis, and H.F. Durrant-Whyte. A low-cost, redundant inertial measurement unit for unmanned air vehicles. *The International Journal of Robotics Research*, 19(11):1089, 2000.

[15] D.H. Titterton, J.L. Weston, and J.L. Weston. *Strapdown inertial navigation technology*. Progress in Astronautics and Aeronautics. American Institute of Aeronautics and Astronautics, 2004.

[16] A. Waegli, S. Guerrier, and J. Skaloud. Redundant MEMS-IMU integrated with GPS for Performance Assessment in Sports. *Position, Location and Navigation Symposium, 2008 IEEE/ION*, 2008.

[17] A. Waegli, J. Skaloud, S. Guerrier, M.E. Parés, and I. Colomina. Noise reduction and estimation in multiple micro-electro-mechanical inertial systems. *Measurement Science and Technology*, 21:065201, 2010.

Vita

Originally from Guatemala, Hector Escobar completed his undergraduate studies in Electrical Engineering in 2005. He moved to Austin, TX in 2008 to start his graduate studies in the Aerospace Engineering Department at the University of Texas at Austin. He worked with Dr. Robert H. Bishop in the development of autonomous rovers. Currently, he is working under the supervision of Dr. Maruthi R. Akella studying optimal configurations of redundant Inertial Measurement Units and expects to complete his Master's in 2010. He will pursue a PHD degree after that.

Permanent address: 612 W North Loop Blvd Apt D
Austin, Texas 78751

This report was typeset with LATEX† by the author.

_____

†LATEX is a document preparation system developed by Leslie Lamport as a special version of Donald Knuth's TEX Program.